Supplementary Information

Structural evolution and strain generation of derived-Cu catalysts during CO_2 electroreduction

Qiong Lei,[†] Liang Huang,[‡,Δ] Jun Yin,[†,Σ] Bambar Davaasuren,[δ] Youyou Yuan,[δ] Xinglong Dong,[†,Σ] Zhi-peng Wu,[†] Xiaoqian Wang,[†] Kexin Yao,[#] Xu Lu,[‡,Δ] Yu Han*[†,Σ]*

[†] Advanced Membranes and Porous Materials Center, Physical Sciences and Engineering Division (PSE), King Abdullah University of Science and Technology (KAUST), Thuwal 23955-6900, Saudi Arabia.

[‡] Clean Combustion Research Center, PSE, KAUST, Thuwal 23955-6900, Saudi Arabia.

[Δ] KAUST Solar Center, PSE, KAUST, Thuwal 23955-6900, Saudi Arabia.

[δ] Imaging and Characterization Core Lab, KAUST, Thuwal 23955-6900, Saudi Arabia.

[Σ] KAUST Catalysis Center, PSE, KAUST, Thuwal 23955-6900, Saudi Arabia.

[#] Multi-scale Porous Materials Center, Institute of Advanced Interdisciplinary Studies, & School of Chemistry and Chemical Engineering, Chongqing University, Chongqing 400044, P. R. China.

Corresponding Author

* yu.han@kaust.edu.sa and xu.lu@kaust.edu.sa

This supplementary information contains:

- Supplementary Note
- Supplementary Figs. 1-18
- Supplementary Tables 1-3
- Supplementary References

Supplementary Note

Before addressing the catalyst evolution during the CO_2RR, we first investigated the redox behavior of the three oxidized Cu samples by performing Cyclic Voltammetry (CV) in 0.1 M KOH aqueous solution. Two reduction peaks were observed in the CV pattern of CuO at 0.57 and 0.32 V_{RHE}, corresponding to the reduction of CuO to Cu_2O and then to Cu, respectively (Supplementary Fig. 5a), which is consistent with the findings of previous studies.[1-2] The reduction peaks corresponding to the reduction of $Cu(OH)_2$ and $Cu_2(OH)_2CO_3$ to Cu_2O were maintained at approximately 0.55 V_{RHE}, whereas those corresponding to the reduction to Cu shifted to 0.11 V_{RHE} (Supplementary Figs. 5b-c). An additional peak was observed at 0.97 V_{RHE}, which could be attributed to the dissociation of $Cu(OH)_2$ or $Cu_2(OH)_2CO_3$ to Cu^{2+}. These results indicate that the electroreduction of $Cu_2(OH)_2CO_3$, $Cu(OH)_2$, and CuO goes through a Cu_2O formation stage, followed by a full reduction to Cu.

Linear Sweep Voltammetry (LSV) was performed on the three oxidized Cu samples in Ar-saturated 0.1 M $KHCO_3$ (Supplementary Fig. 5d). Two intense peaks were observed in the LSV curve of CuO at -0.16 and -0.58 V_{RHE}, which corresponded to the reduction of CuO to Cu_2O and then to Cu, respectively, whereas only one broad reduction peak was observed on $Cu_2(OH)_2CO_3$ at -0.96 V_{RHE}, and two broad reduction peaks on $Cu(OH)_2$ at -0.69 and -1.18V_{RHE}. These results indicate that in both KOH and $KHCO_3$ environments, the electroreduction of $Cu_2(OH)_2CO_3$ and $Cu(OH)_2$ to Cu required more negative potentials compared to that of CuO. It is important to note that the data presented here are the first LSV scans of each freshly prepared electrode; therefore, the current density and potential cannot directly correlate with those in the discussion of the CO_2RR performance of the catalysts, because the electroreduction kinetics of oxidized Cu phases can be slow on the time scale of CO_2RR[3] (details will be discussed in the subsequent paragraphs in the main text).

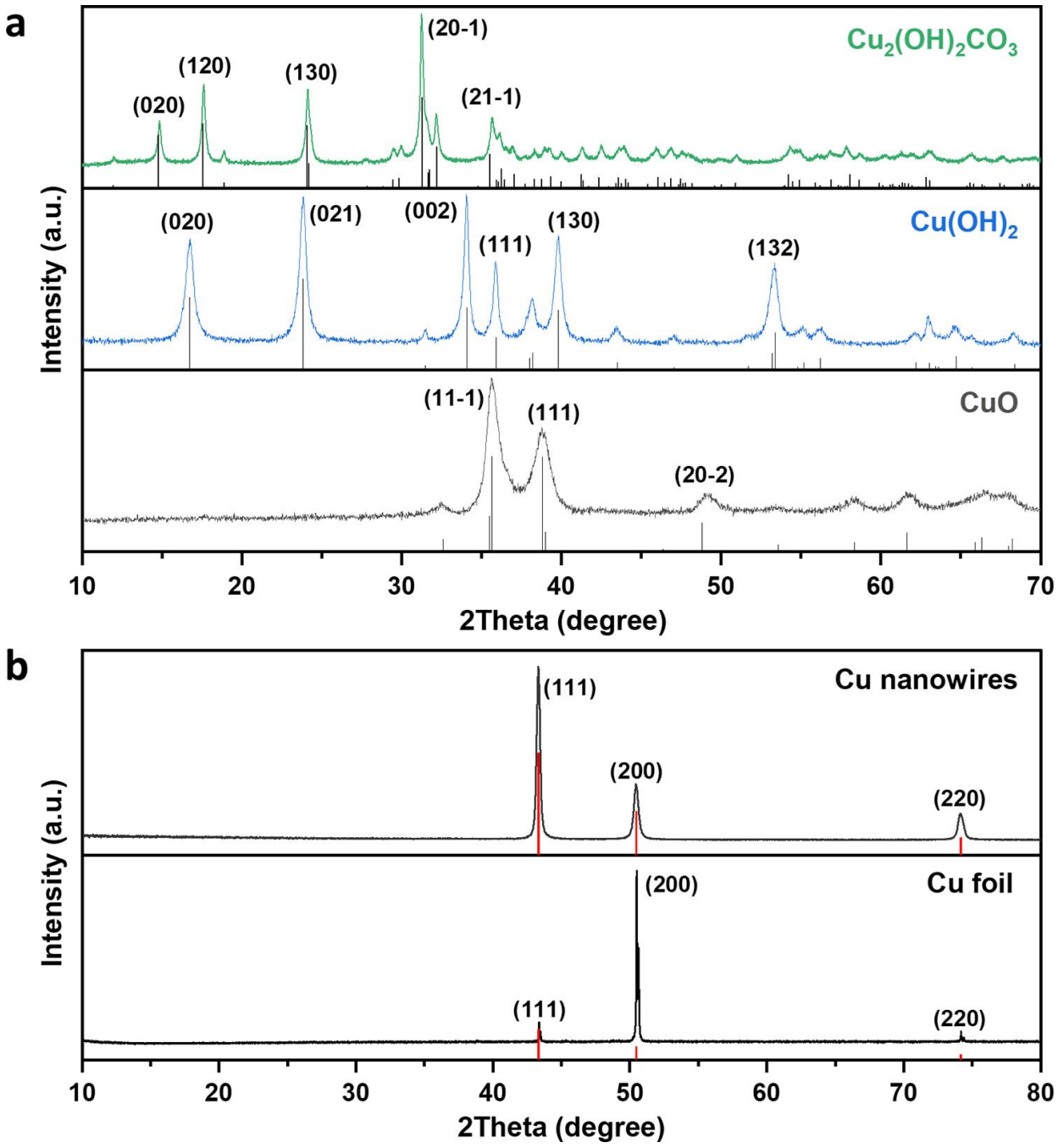

Supplementary Fig. 1. Indexed *ex situ* XRD patterns of (a) $Cu_2(OH)_2CO_3$, $Cu(OH)_2$, and CuO nanocrystals, and (b) Cu nanowires and polycrystalline Cu foil.

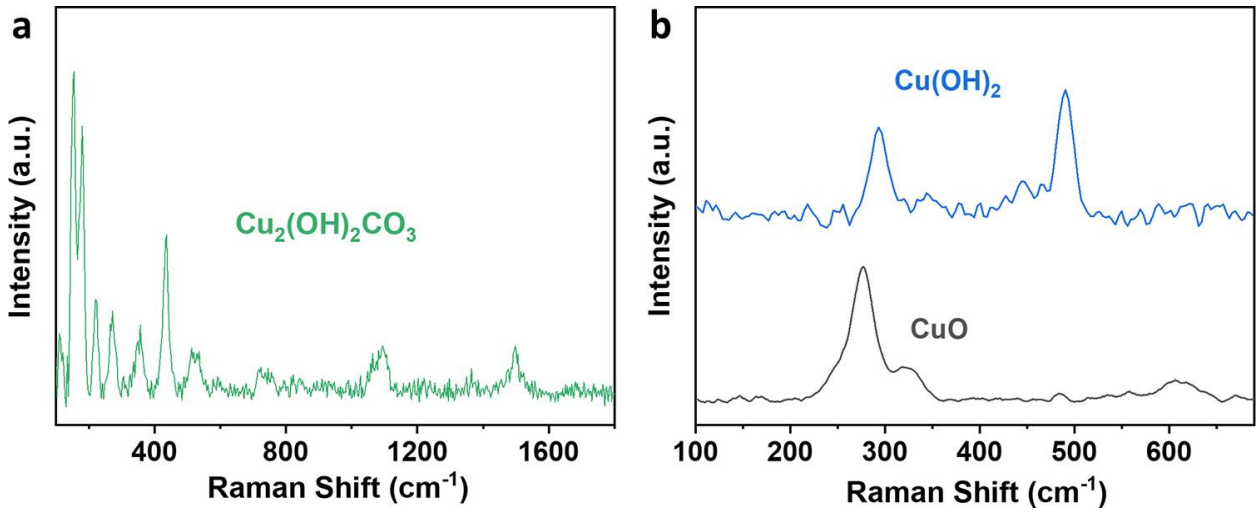

Supplementary Fig. 2. *Ex situ* Raman spectra of (a) $Cu_2(OH)_2CO_3$, and (b) $Cu(OH)_2$ and CuO nanocrystals.

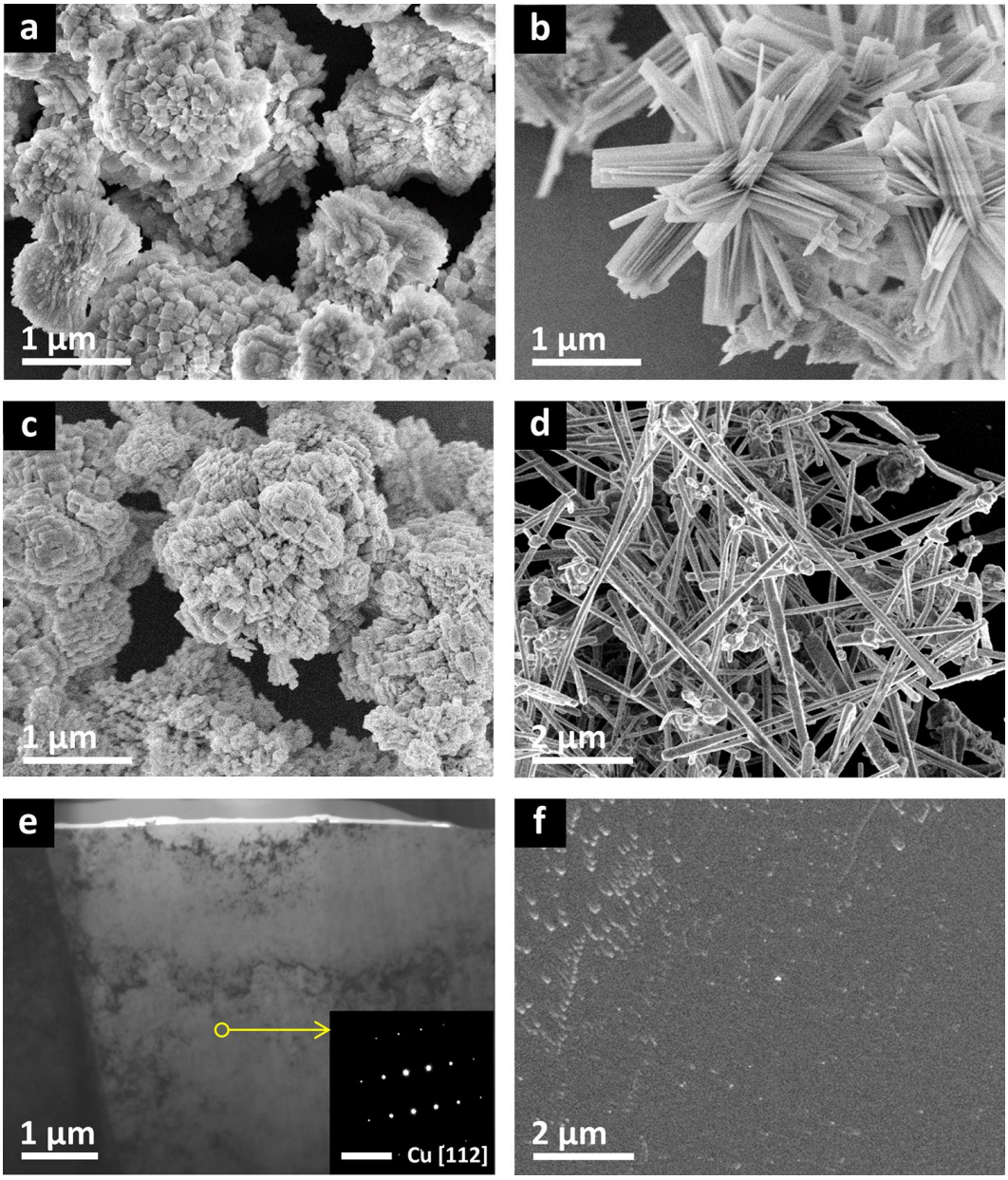

Supplementary Fig. 3. SEM images of (a) $Cu_2(OH)_2CO_3$, (b) $Cu(OH)_2$, (c) CuO nanocrystals, (d) Cu nanowires, and (f) polycrystalline Cu foil. (e) TEM image of focused ion beam (FIB)-fabricated specimen from electropolished Cu foil. The corresponding SAED pattern (inset, scale bar 10 1/nm) was collected in the circled area with a diameter of ~160 nm. FIB was performed using the standard lift-out technique on a dual-beam FIB-SEM (FEI, Helios Nanolab Dualbeam) equipped with an OmniProbe micromanipulator to prepare ultrathin (~100 nm) lamella from the electrode for TEM analysis on the cross-section. The prepared lamella was mounted to a copper half-grid and immediately transferred to glovebox for storage.

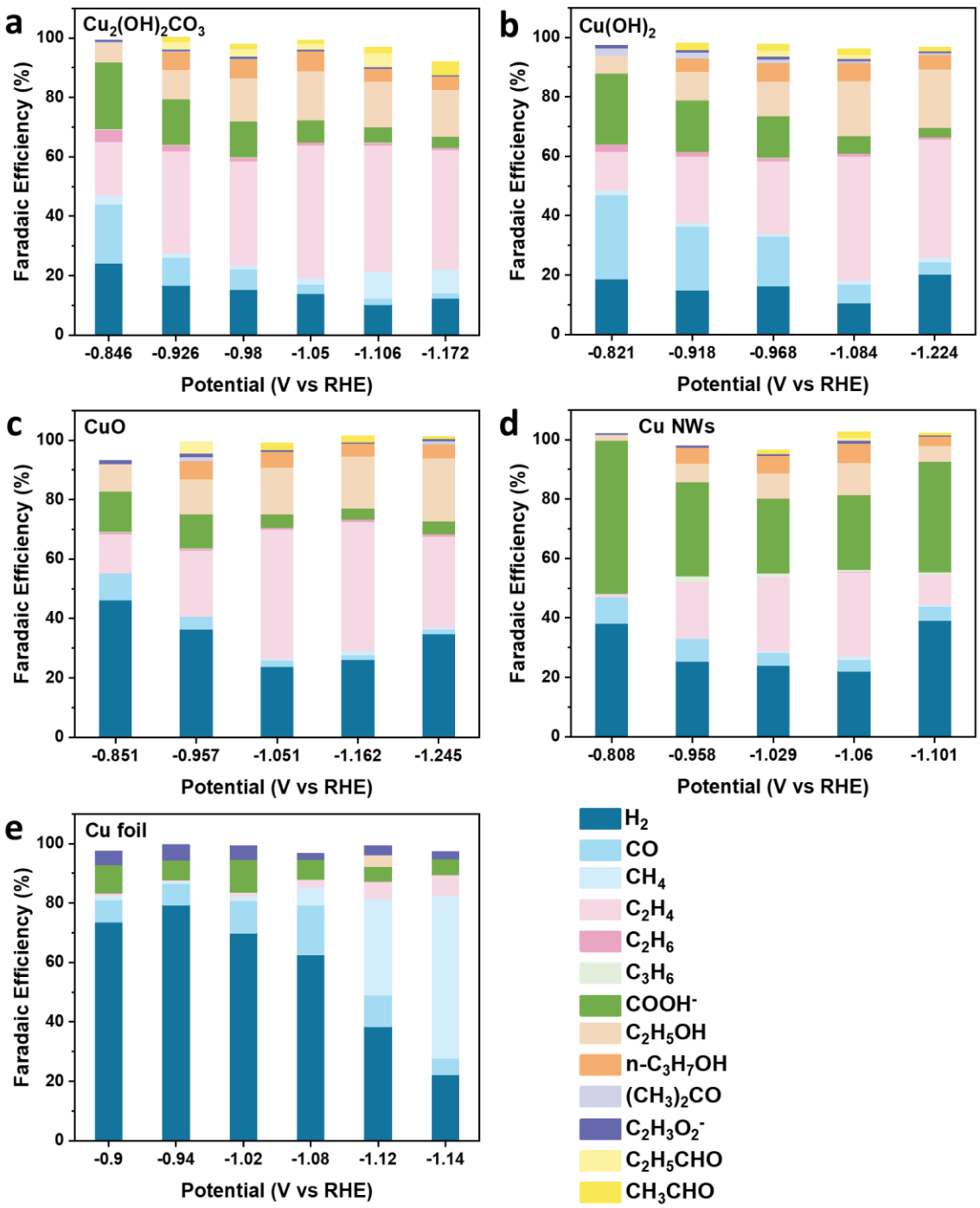

Supplementary Fig. 4. Product distribution for the CO_2RR with (a) $Cu_2(OH)_2CO_3$, (b) $Cu(OH)_2$, (c) CuO nanocrystals, (d) Cu nanowires, and (e) polycrystalline Cu foil at different potentials.

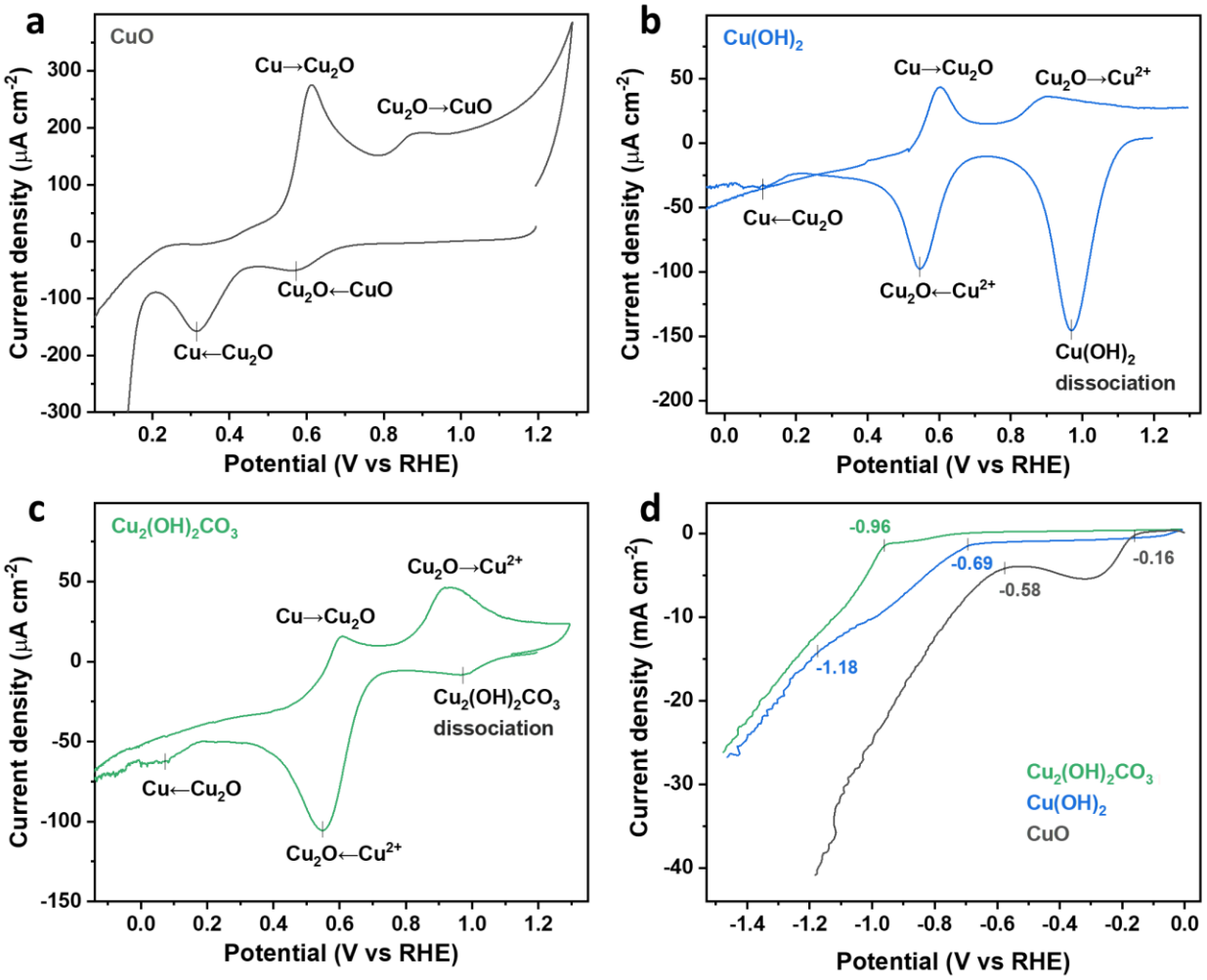

Supplementary Fig. 5. Cyclic Voltammetry (CV) of (a) CuO, (b) $Cu(OH)_2$, and (c) $Cu_2(OH)_2CO_3$ nanocrystals in 0.1 M KOH. (d) Linear Sweep Voltammetry (LSV) with these three catalysts in Ar-saturated 0.1 M $KHCO_3$. Potential sweep rate was 5 mV s^{-1}.

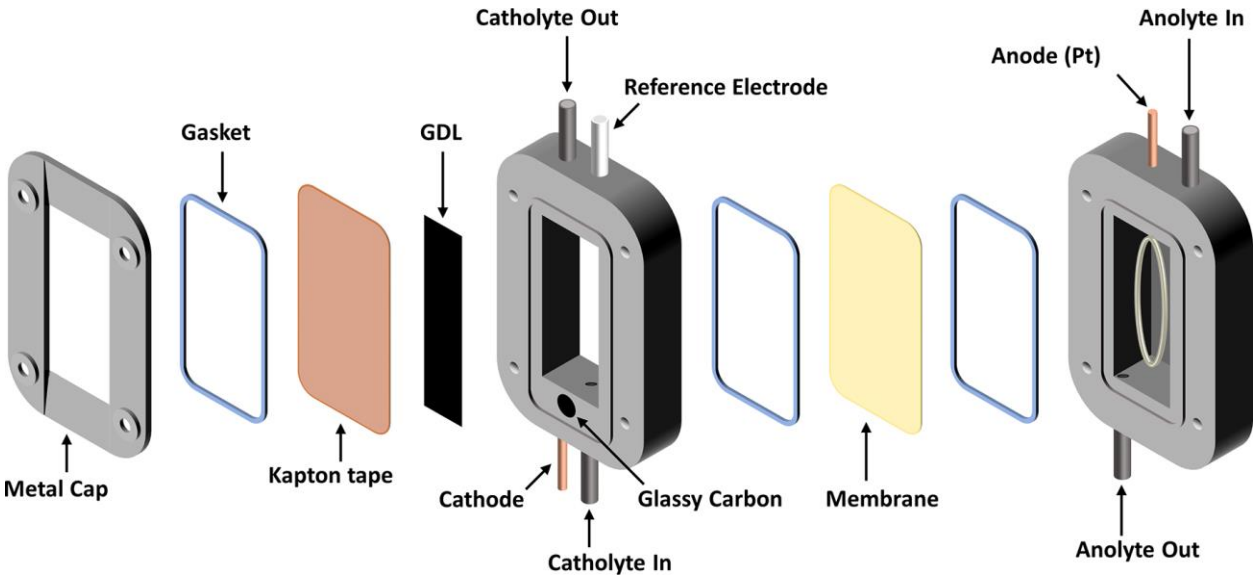

Supplementary Fig. 6. Exploded view of the customized cell for *operando* XRD characterization under CO_2RR conditions.

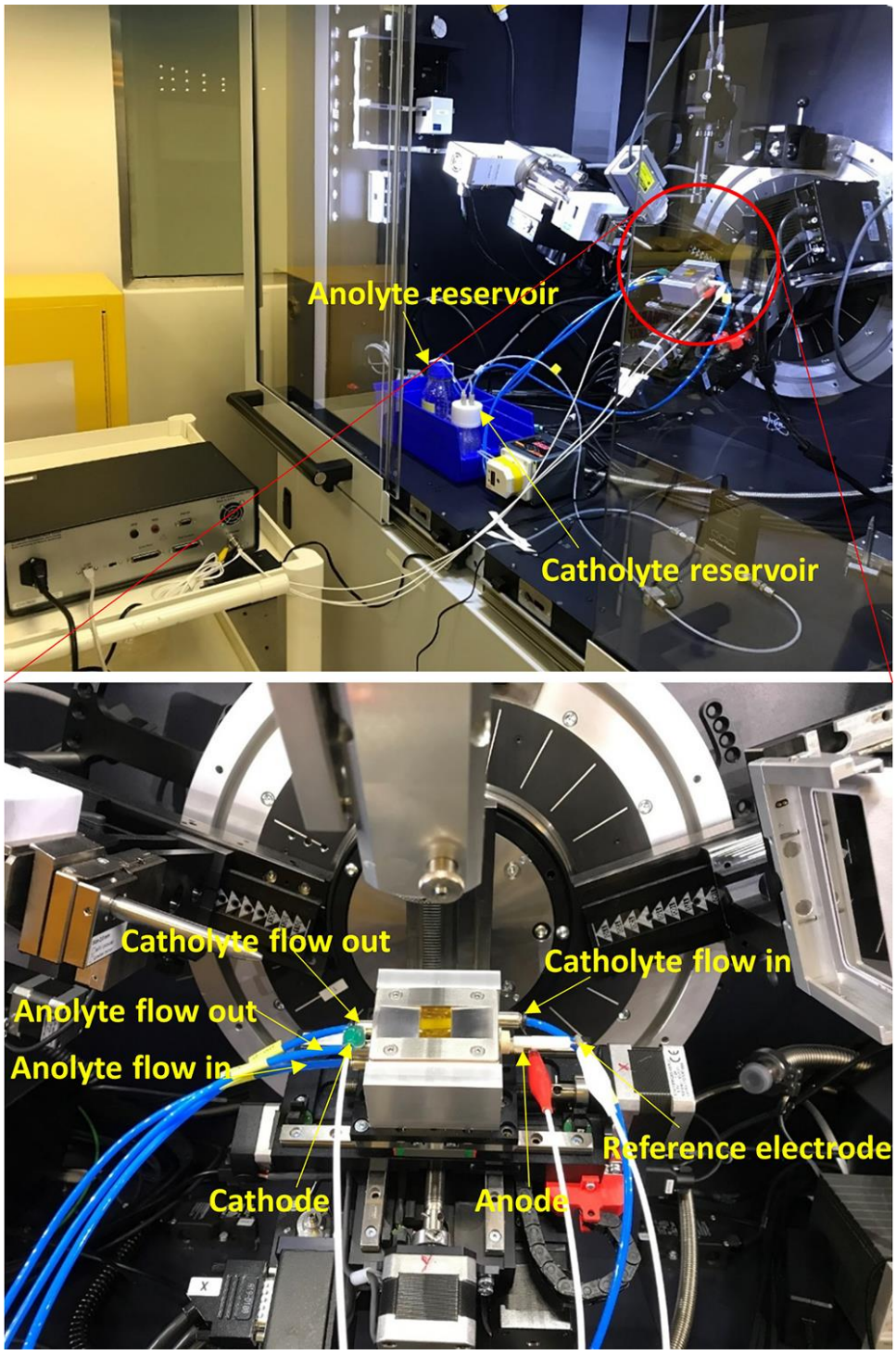

Supplementary Fig. 7. Setup for the *operando* XRD under the CO_2RR conditions.

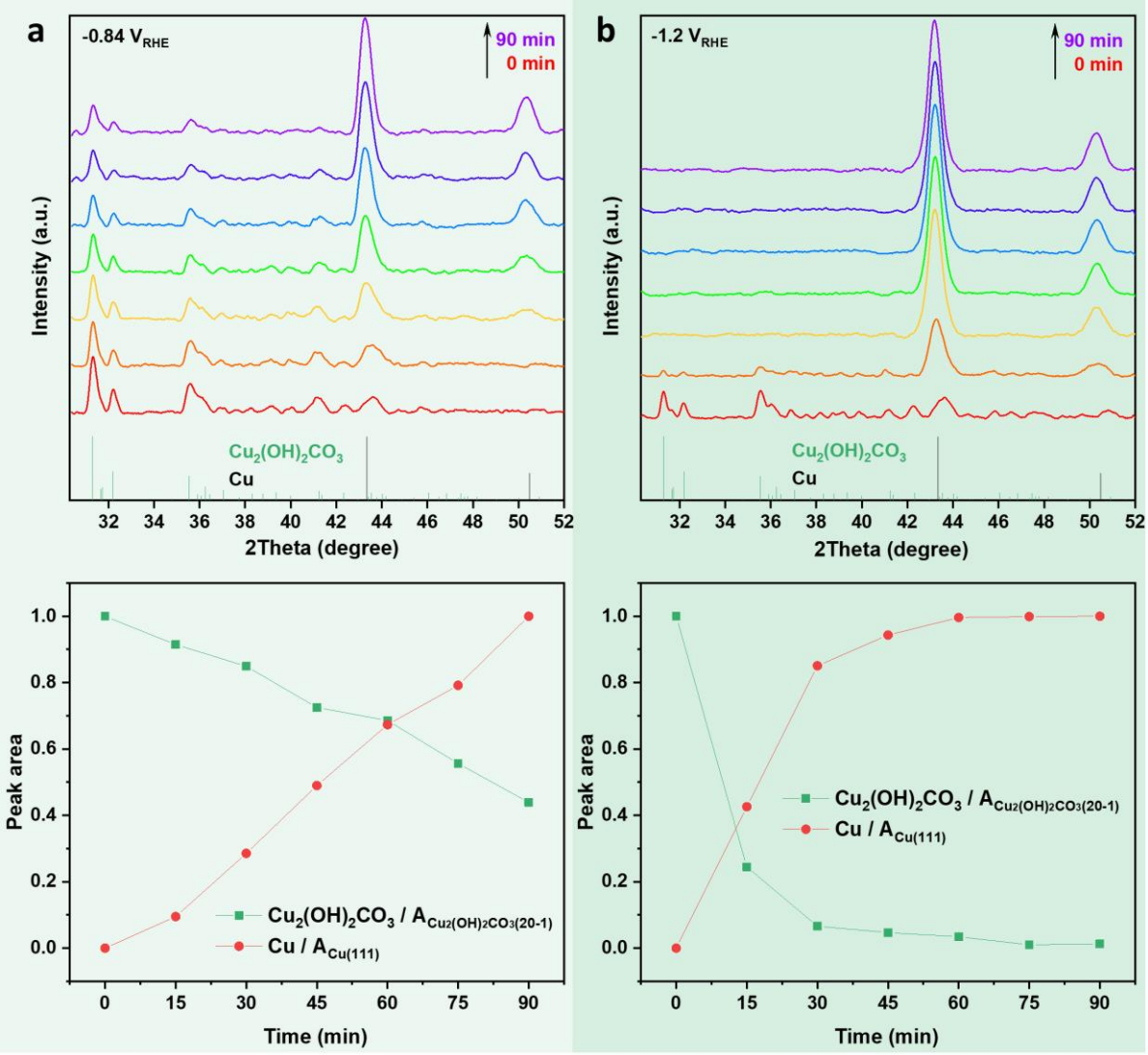

Supplementary Fig. 8. Time-resolved *operando* XRD patterns (upper panel) and the corresponding quantitative peak analysis (lower panel) for the CO_2RR with $Cu_2(OH)_2CO_3$ at (a) -0.84 V_{RHE} and (b) -1.2 V_{RHE}. Spectra were collected every 15 min. For the quantitative peak analysis, the integrated and normalized intensities of $Cu_2(OH)_2CO_3$(20-1) and Cu(111) were used.

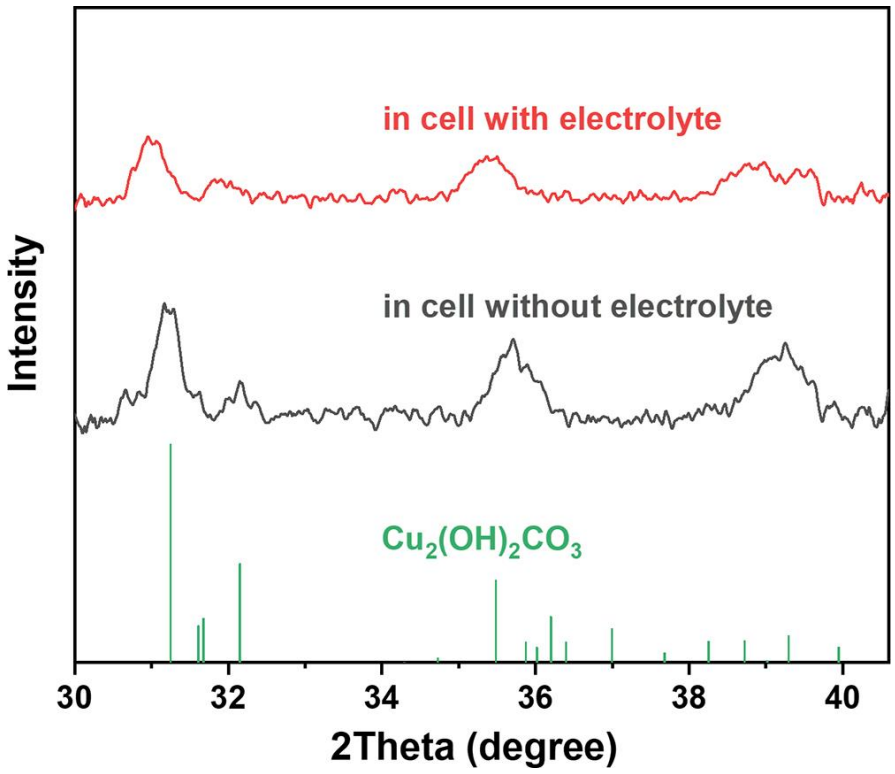

Supplementary Fig. 9. Comparison for the XRD patterns of $Cu_2(OH)_2CO_3$ electrode in fully assembled cell with and without electrolyte. Other parameters were kept same for the measurements.

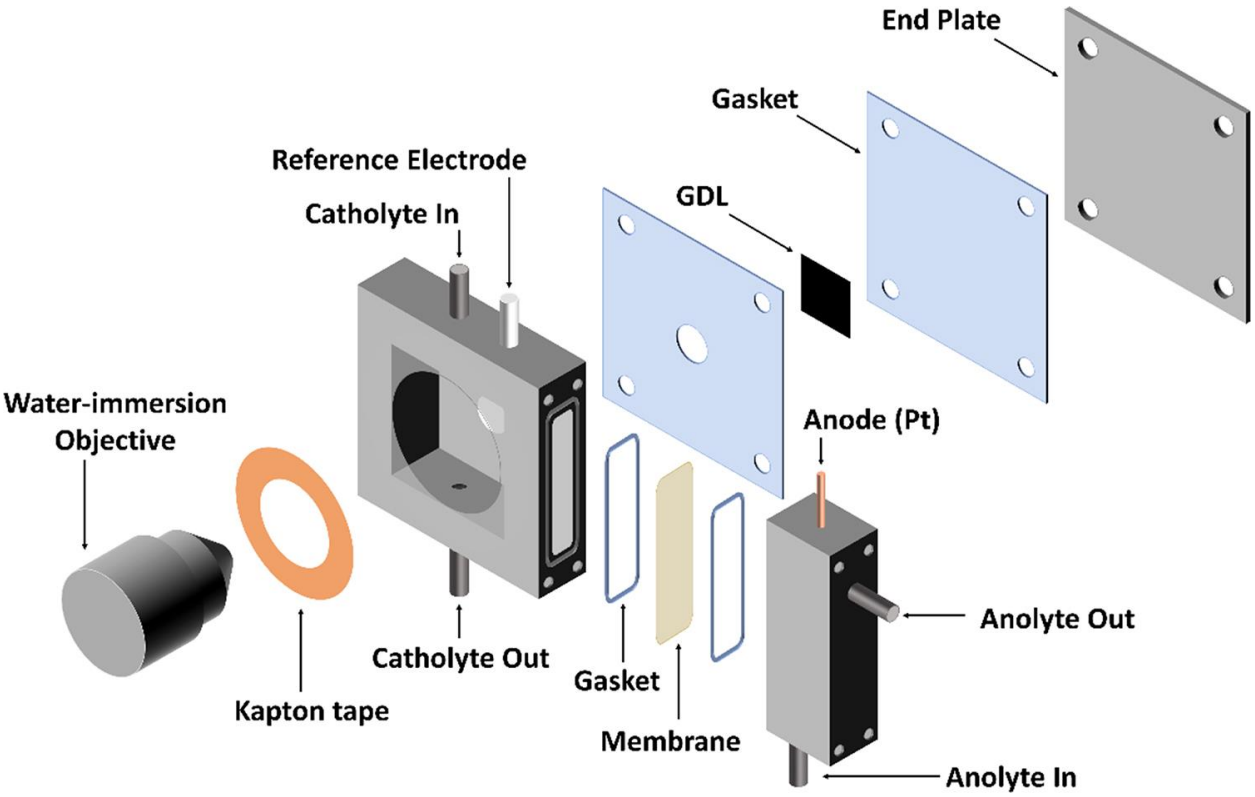

Supplementary Fig. 10. Exploded view of the customized cell for *operando* Raman characterization under CO_2RR conditions.

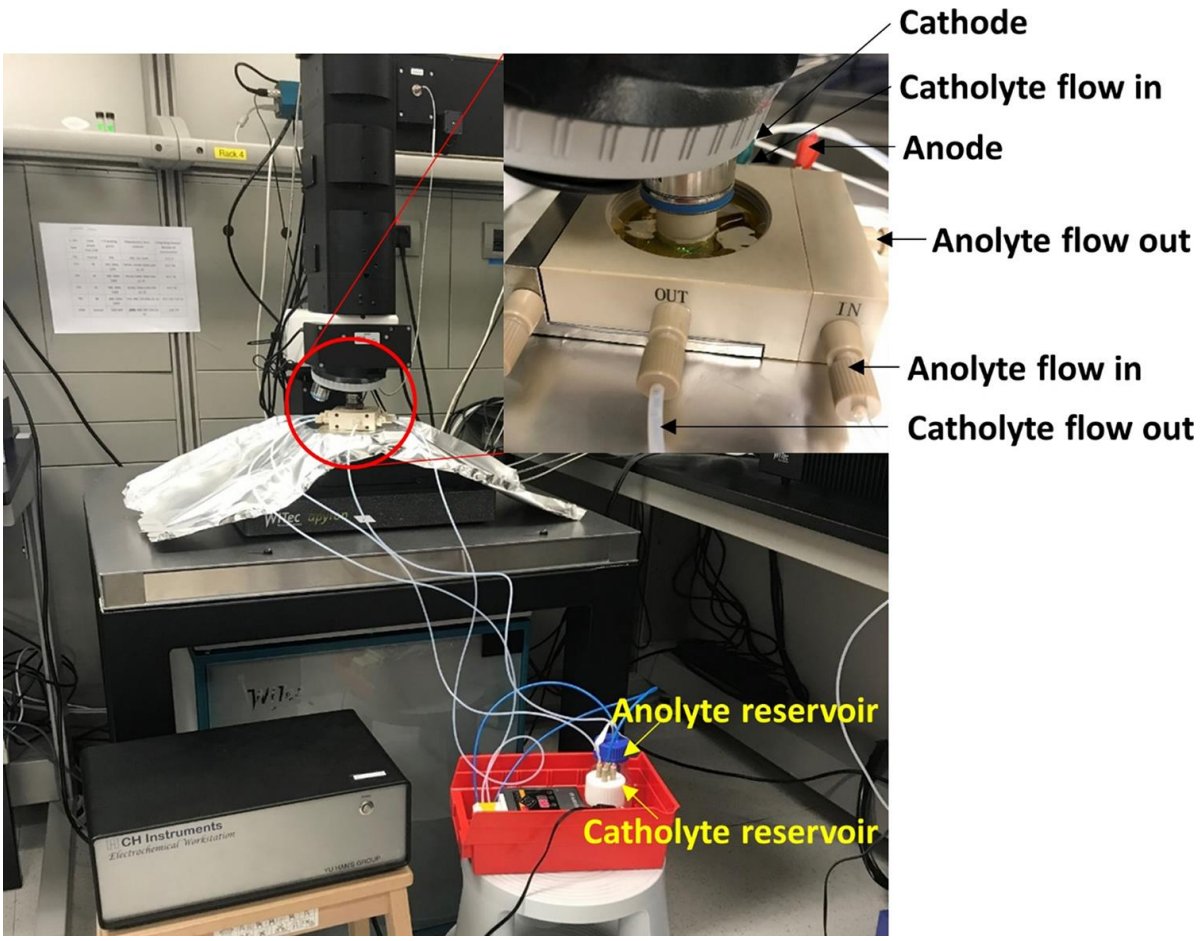

Supplementary Fig. 11. Setup for the *operando* Raman spectroscopy under the CO_2RR conditions.

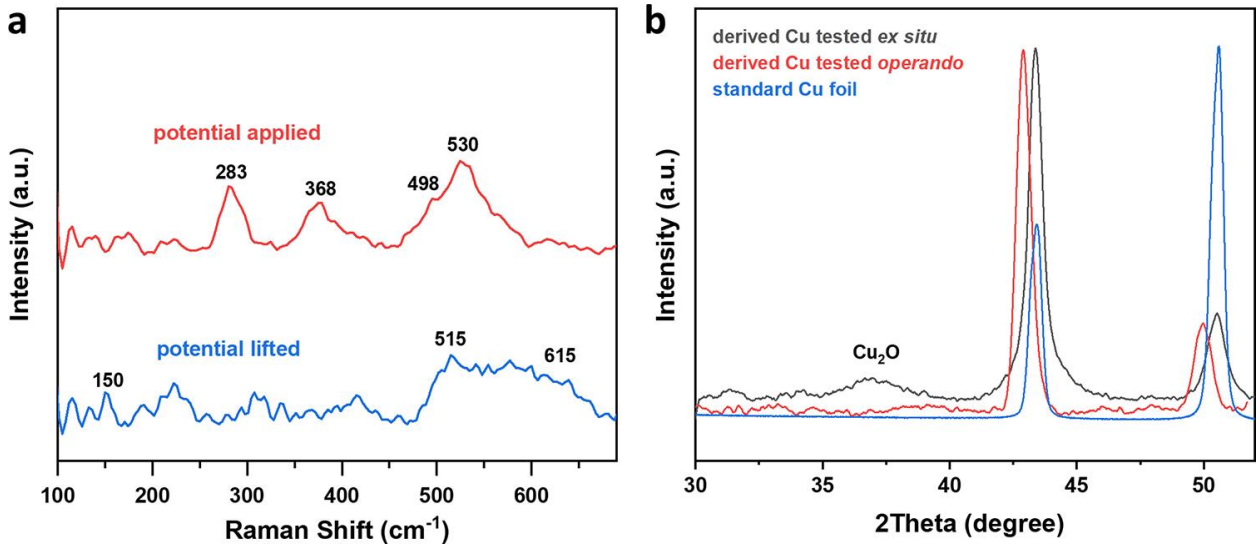

Supplementary Fig. 12. (a) Comparison for the Raman spectra collected when applying and then lifting the potential during the CO_2RR with CuO nanocrystals at -1.16 V_{RHE}. Other parameters were kept same for the measurements. (b) Comparison for the XRD patterns collected *operando* and *ex situ* (electrode removed from electrolyte and dried with N_2) during (or after) the CO_2RR with $Cu_2(OH)_2CO_3$ nanocrystals at -1.05 V_{RHE} for 1.5 h. Cu foil was tested on the same XRD instrument as a reference.

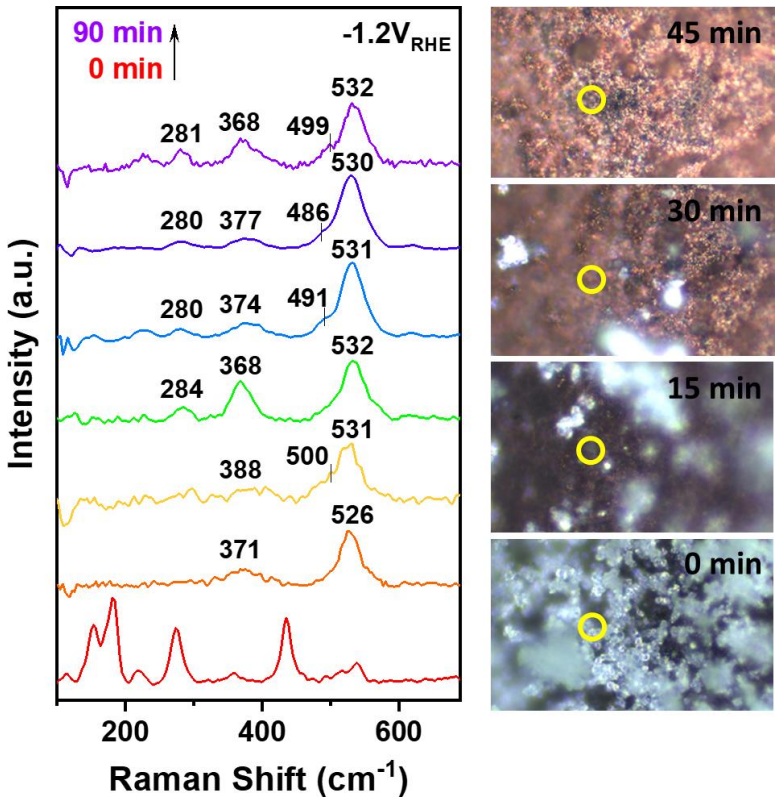

Supplementary Fig. 13. Time-resolved *operando* Raman spectra (left panel) and light microscopy (right panel) for the CO_2RR with $Cu_2(OH)_2CO_3$ at -1.2 V_{RHE}. Spectra were collected every 15 min.

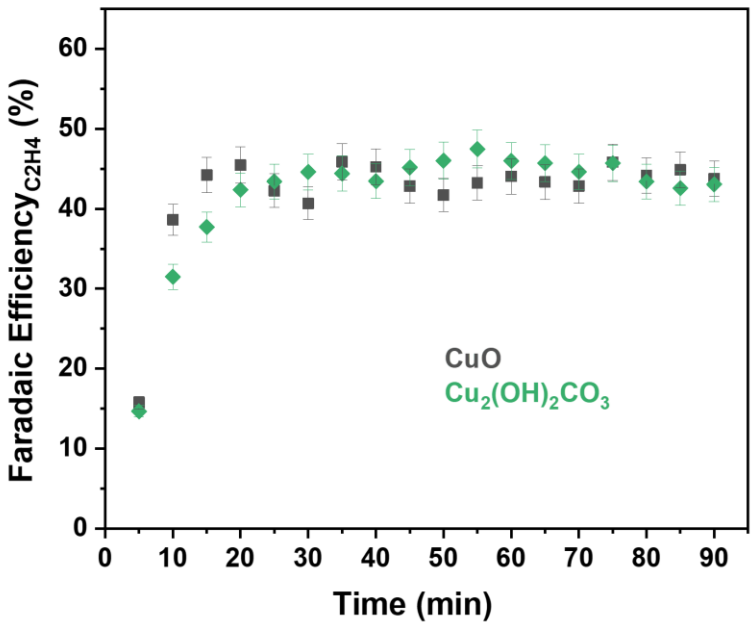

Supplementary Fig. 14. $FE_{C_2H_4}$ of the $Cu_2(OH)_2CO_3$ and CuO nanocrystals at -1.05 and -1.16 V_{RHE}, respectively. Both CO_2RR experiments were performed in an H-type cell using CO_2-saturated 0.1 M $KHCO_3$ as the electrolyte for 1.5 h.

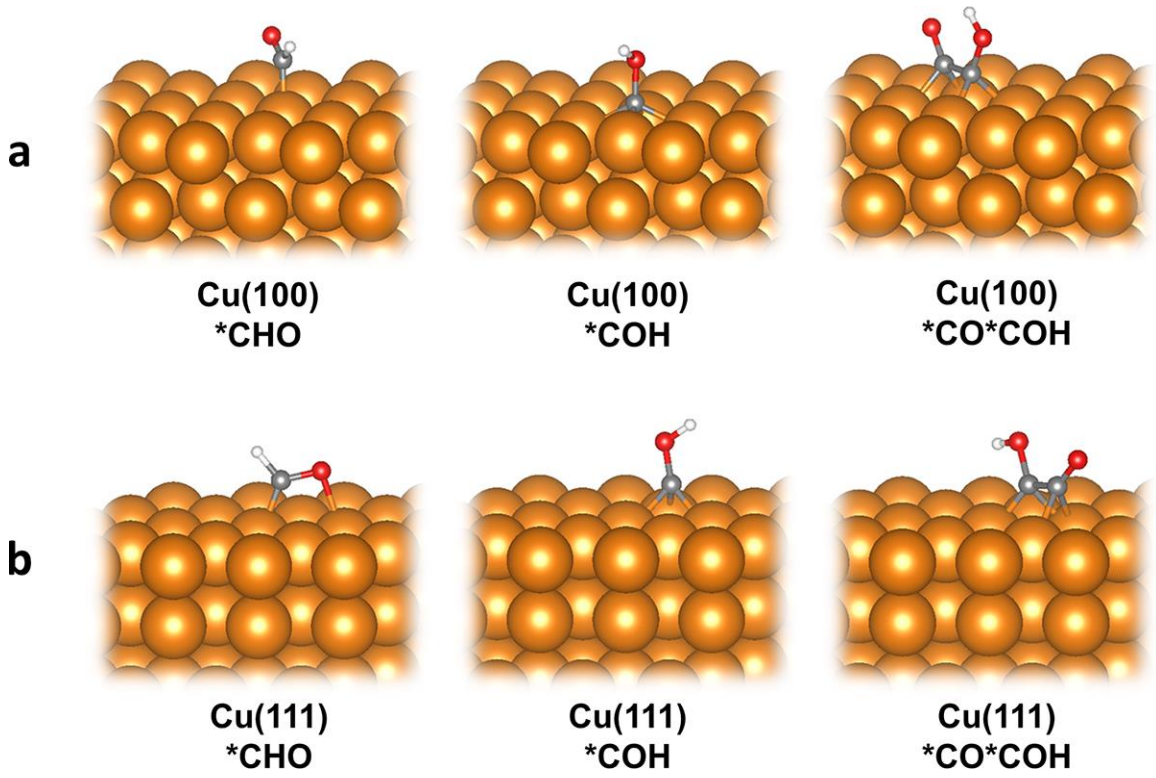

Supplementary Fig. 15. Optical crystal structures for (a) strain-free Cu(100) and (b) strain-free Cu(111) with *CHO, *COH, and *CO*COH adsorption.

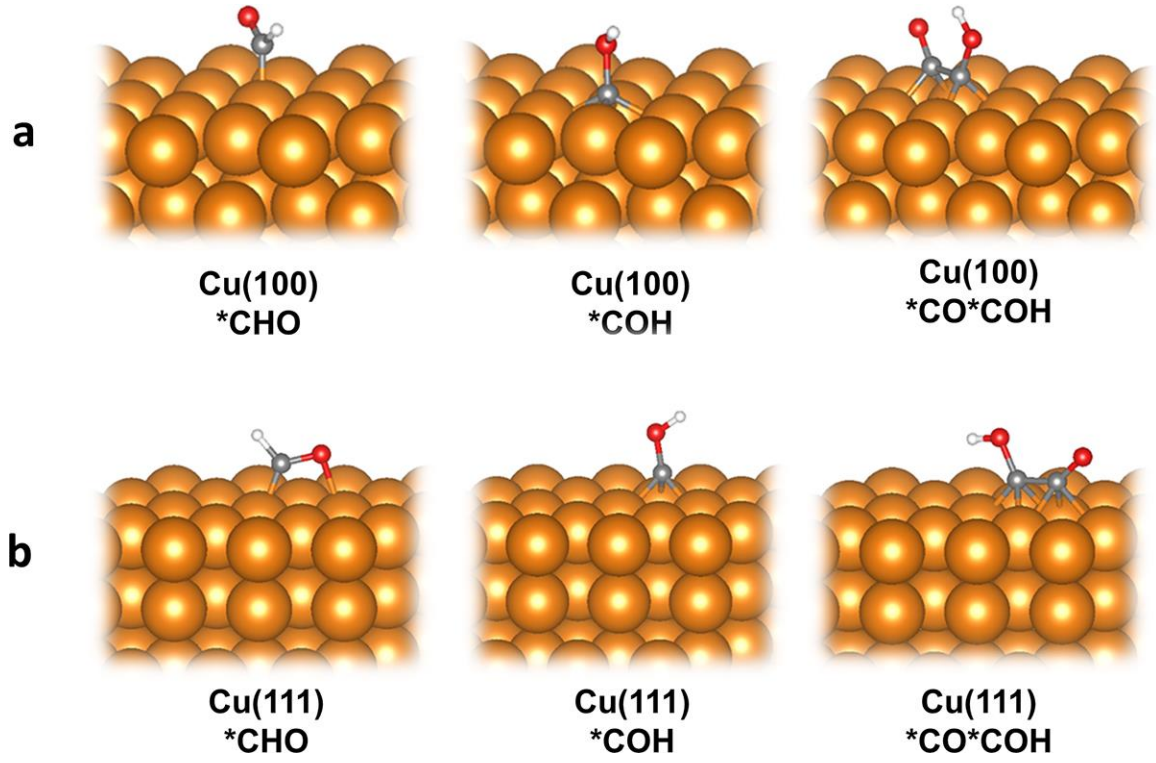

Supplementary Fig. 16. Optical crystal structures for (a) Cu(100) with 0.72% tensile strain and (b) Cu(111) with 0.55% tensile strain with *CHO, *COH, and *CO*COH adsorption.

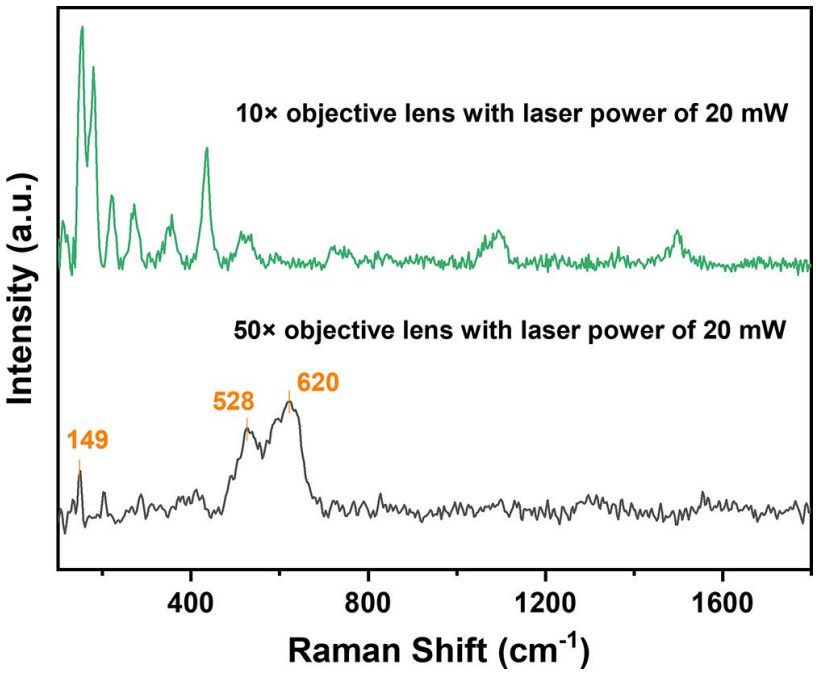

Supplementary Fig. 17. Raman spectra acquired with high (50x) and low (10x) magnification objective lenses during the *ex situ* Raman characterization for the $Cu_2(OH)_2CO_3$ nanocrystals. Other parameters were kept the same for the measurements.

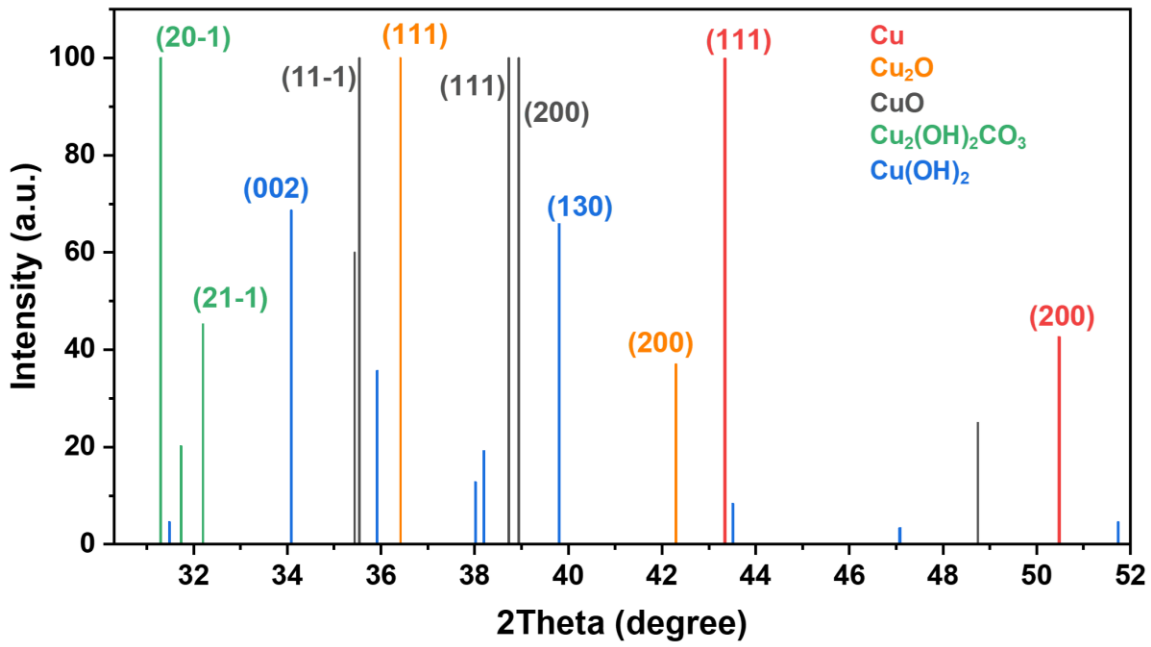

Supplementary Fig. 18. 2Theta range of interest for the *operando* XRD measurements under CO_2RR conditions.

Supplementary Table 1. Crystal size estimation using Scherrer equation.

Sample	$Cu_2(OH)_2CO_3$	$Cu(OH)_2$	CuO
Initial mean crystal size (nm)	24.7 ± 3.5	19 ± 0.5	10 ± 0.5
Derived mean crystal size (nm)	11.8 ± 1.7	11.7 ± 1.4	11.6 ± 1.4

Supplementary Table 2. Diffraction peak shifts and the corresponding lattice parameters and strain values observed during the *operando* XRD on $Cu_2(OH)_2CO_3$, $Cu(OH)_2$, and CuO nanocrystals at different CO_2RR potentials. Cu foil was tested on the same XRD instrument as a reference.

Cu precursor	CO_2RR potential (V_{RHE})	Cu(111)			Cu(200)		
		Average XRD peak position (2theta)	Lattice parameter (Å)	Strain (%)	Average XRD peak position (2theta)	Lattice parameter (Å)	Strain (%)
$Cu_2(OH)_2CO_3$	-0.84	43.1586	3.6305	**0.51**	50.1611	3.6373	**0.67**
	-1.05	43.1410	3.6319	**0.55**	50.1313	3.6394	**0.72**
	-1.20	43.1097	3.6345	**0.61**	50.1414	3.6387	**0.70**
$Cu(OH)_2$	-0.63	43.1953	3.6276	**0.42**	50.2687	3.6301	**0.46**
	-0.83	43.1751	3.6292	**0.47**	50.2565	3.6309	**0.49**
	-1.08	43.1912	3.6279	**0.43**	50.2526	3.6311	**0.49**
CuO	-0.82	43.3870	3.6123	**0.00**	50.5121	3.6137	**0.01**
	-1.16	43.3602	3.6145	**0.06**	50.4813	3.6158	**0.07**
	-1.23	43.3810	3.6128	**0.02**	50.4422	3.6184	**0.14**
Cu foil	-	43.3881	3.6123	**0**	50.5186	3.6133	**0**

Supplementary Table 3. Unit-cell volumes of the three oxidized Cu catalysts and the corresponding cell volume reduction after their electroreduction to Cu.

Sample	Unit-cell volume ($Å^3$)	Cu atoms per unit-cell	Cell volume per 4 Cu atoms ($Å^3$)	Cell volume reduction per 4 Cu atoms (%)
$Cu_2(OH)_2CO_3$	364.35	8	182.175	74
$Cu(OH)_2$	164.14	4	164.14	71
CuO	81.08	4	81.08	42
Cu	47.16	4	47.16	-

References

(1) Bohme, A.; Sterl, F.; Kath, E.; Ubl, M.; Manninen, V.; Giessen, H. Electrochemistry on Inverse Copper Nanoantennas: Active Plasmonic Devices with Extraordinarily Large Resonance Shift. *ACS Photonics* **2019,** *6*, 1863-1868.
(2) Caballero-Briones, F.; Artes, J. M.; Diez-Perez, I.; Gorostiza, P.; Sanz, F. Direct Observation of the Valence Band Edge by in Situ ECSTM-ECTS in p-Type Cu_2O Layers Prepared by Copper Anodization. *Journal of Physical Chemistry C* **2009,** *113*, 1028-1036.
(3) Henckel, D. A.; Counihan, M. J.; Holmes, H. E.; Chen, X. Y.; Nwabara, U. O.; Verma, S.; Rodriguez-Lopez, J.; Kenis, P. J. A.; Gewirth, A. A. Potential Dependence of the Local pH in a CO_2 Reduction Electrolyzer. *ACS Catalysis* **2021,** *11*, 255-263.